Simulations of the Eastern North Pacific Intraseasonal Variability in CMIP5 GCMs

Xian-an Jiang[1,2], Eric D. Maloney[3], Jui-Lin F. Li[2], and Duane E. Waliser[2]

[1]*Joint Institute for Regional Earth System Science & Engineering, University of California, Los Angeles, California*

[2]*Jet Propulsion Laboratory, California Institute of Technology, Pasadena, California*

[3]*Department of Atmospheric Science, Colorado State University, Fort Collins, Colorado*

Submitted to Journal Climate, July 30, 2012

Corresponding author address: Dr. Xianan Jiang, Jet Propulsion Laboratory, California Institute of Technology, MS 233-300, 4800 Oak Grove Dr., Pasadena, CA 91109. Email: xianan@jifresse.ucla.edu.

Copyright © 2012. All rights reserved.

Abstract

As a key component of tropical atmospheric variability, intraseasonal variability (ISV) over the eastern north Pacific (ENP) exerts pronounced influences on regional weather and climate. Since general circulation models (GCMs) are essential tools for prediction and projection of future climate, current model deficiencies in representing this important variability leave us greatly disadvantaged in studies and prediction of climate change. In this study, we have assessed model fidelity in representing ENP ISV by analyzing sixteen GCMs participating in the fifth phase of the Coupled Model Inter-comparison Project (CMIP5). Among the sixteen CMIP5 GCMs examined in this study, only seven GCMs capture the spatial pattern of the leading ENP ISV mode relatively well, although even these several GCMs exhibit biases in simulating ISV amplitude. Analyses indicate that model fidelity in representing ENP ISV is closely associated with ability to simulate a realistic summer mean state. The presence of westerly or weak mean easterly winds over the ENP warm pool region could be conducive for more realistic simulations of the ISV. One hypothesis to explain this relationship is that a realistic mean state could produce the correct sign of surface flux anomalies relative to the ISV convection, which helps to destabilize local intraseasonal disturbances. The projected changes in characteristics of ENP ISV under the RCP8.5 projection scenario are also explored based on simulations from four CMIP5 GCMs. Results suggest that, in a future climate, the amplitude of ISV could be enhanced over the southern part of the ENP, while reduced over the northern ENP off the coast of Mexico/Central America and the Caribbean.

1. Introduction

During boreal summer, convective activity over the eastern north Pacific (ENP) along the intertropical convergence zone (ITCZ) exhibits significant intraseasonal variability (ISV). Through its associated large-scale circulation and thermodynamical variations, the ISV exerts broad impacts on regional weather and climate systems, including the North American Monsoon, mid-summer drought over central America, Caribbean rainfall and low-level jet, as well as tropical cyclone activity over the ENP and the Gulf of Mexico (e.g., Magana et al. 1999; Maloney and Hartmann 2000a, 2000b; Higgins and Shi 2001; Lorenz and Hartmann 2006; Small et al. 2007; Wu et al. 2009; Serra et al. 2010; Martin and Schumacher 2010). By modulating the activity of these climate / weather systems on an intraseasonal time scale, the ISV thus provides a foundation for extended-range prediction of the tropical atmosphere.

Two leading ISV modes associated with the ENP ITCZ have been previously reported with dominant periods of 40 days (hereafter a 40-day ISV mode) and 16 days (i.e., a quasi-biweekly mode, QBM), respectively. The 40-day ISV mode over the ENP is largely considered a local expression of the global Madden-Julian Oscillation (MJO; Madden and Julian 1994; e.g., Maloney and Esbensen 2003), although recent modeling work suggests that similar 40-day ENP variability can exist when isolated from the Eastern Hemisphere (Rydbeck et al. 2012). In addition to the eastward propagation, a northward-moving component of this mode is also noted (Jiang and Waliser 2008; Maloney et al. 2008; Small et al. 2011), exhibiting substantial similarity to its counterpart in the Asian summer monsoon (Jiang et al. 2004; Jiang and Waliser 2008). The second leading ISV mode over the ENP (i.e., QBM) exhibits a smaller spatial scale than the first ISV mode, and is largely characterized by meridional propagation (Jiang and Waliser 2009).

While significant achievements have been made in modeling global ISV during past decades, significant challenges remain in current general circulation models (GCMs; e.g., Slingo et al. 1996; Waliser et al. 2003; Lin et al. 2006; Kim et al. 2009). For ENP ISV, by applying an extended empirical orthogonal function (EEOF) technique, a recent analysis including many CMIP3-era models illustrated that among the total nine models examined, only two GCMs were able to realistically simulate both of the two observed leading ISV modes over the ENP (Jiang et al. 2011). Deficiencies of current GCMs in representing this important form of variability greatly limit our skill for extended-range prediction. Until very recently, useful predictive skill of the global ISV in most current GCMs had generally been limited to only 1–2 weeks (Waliser 2011), although the intrinsic period of the dominant mode of intraseasonal variability is about 40-50 days. Meanwhile, as GCMs have been essential tools for prediction and projection of climate changes, large model deficiencies in depicting this fundamental component of atmospheric variability leave us disadvantaged in undertaking climate change studies, particularly in projecting future activities of extreme events that are significantly modulated by ISV.

Building upon past successes of several model comparison project activities, the fifth phase of the Coupled Model Intercomparison Project (CMIP5) provides another state-of-the-art multi-model dataset to advance our knowledge of climate variability and climate change (Taylor et al. 2012). In this study, we assess CMIP5 model fidelity in representing ISV over the ENP and neighboring areas by analyzing sixteen GCMs participating in CMIP5. This work is a part of the collective efforts coordinated by the CMIP5 Task Force of the US National Oceanic and Atmospheric Administration (NOAA) Modeling Analysis and Prediction Program (MAPP).

The outline of this paper is as follows. In Section 2, the CMIP5 models and observational datasets used for this study are briefly described. In Section 3, we focus on

examining how well the summer mean state and the leading ISV mode over the ENP are simulated by the sixteen CMIP5 GCMs. We further analyze the projected changes in characteristics of ENP ISV in future climate based on simulations from four GCMs under the RCP8.5 projection scenario. Finally, a summary is presented in Section 5.

2. Model, Datasets, and Approaches

2.1 CMIP5 Models

The CMIP5 experiments were conducted with more than 50 climate models representing 20 modeling groups with the aim of furthering our understanding past and future climate change in key areas of uncertainty (Taylor et al. 2012). In this study, simulations from sixteen atmosphere-ocean GCMs (AOGCMs) using a "historical" scenario are analyzed for the period of 1981-2005 to explore model fidelity in representing ENP ISV in current climate. The historical forcings used to generate these runs include estimates of changes in atmospheric composition from natural and anthropogenic sources, volcanoes, greenhouse gases and aerosols, as well as changes in solar output and land cover. The model names, institutes, and horizontal resolutions of the sixteen AOGCMs used in our study are listed in Table 1. Additionally, simulations from four GCMs under the RCP8.5 projection scenario for the period of 2076-2099 are analyzed to examine projected changes in the ENP ISV in future climate. The main variables analyzed in this study include precipitation, surface latent heat flux, and 850hPa winds.

2.2 Observational datasets

Rainfall observations are based on the Tropical Rainfall Measuring Mission (TRMM, version 3B42 V6; Huffman et al. 1995) precipitation dataset during the period from 1998 to 2010. TRMM 3B42 rainfall is a global precipitation product based on multi-satellite and rain

gauge analyses. It provides precipitation estimates with 3-hourly temporal resolution on a 0.25-degree spatial resolution grid in a global belt between 50°S and 50°N. Daily wind fields during the period of the TRMM rainfall observations are obtained from the recent European Centre for Medium-Range Weather Forecasts (ECMWF) reanalysis, e.g., ERA-Interim (Dee et al. 2011; hereafter ERA-I reanalysis), which have a horizontal grid resolution of 1.5^{o} by 1.5^{o}. Daily estimates of global latent heat flux fields on a one-degree grid generated by the Woods Hole Oceanographic Institution (WHOI) Objectively Analyzed air-sea Fluxes (OAFlux) Project (Yu et al. 2008) are also analyzed to validate model latent heat flux patterns. The OAFlux product is determined from using the best-possible estimates of flux-related surface meteorology and state-of-the-art bulk flux parameterizations (Yu et al. 2008). Several satellite products are utilized in the OAFlux synthesis, including wind speed retrievals from both scatterometer (QuikSCAT) and radiometer (SSM/I, Special Sensor Microwave Imager; and AMSR-E, Advanced Microwave Scanning Radiometer - Earth Observing System) microwave remote sensing, and SST daily high-resolution blended analysis by Reynolds et al. (2007), as well as a near-surface humidity product that was derived from SSM/I column water vapor retrievals (Chou et al. 2001).

A common period of 1998-2010 is used for the observations due to the relatively short record of TRMM rainfall dataset. In addition, all daily variables based on both observations and model simulations were interpolated to a common 2.5^{o} by 2.5^{o} grid system.

3. Simulations of the ENP ISV in CMIP5 GCMs under a historical scenario

3.1 Summer Mean State

In this part of the study, model fidelity in representing the summer mean state over the ENP and adjacent regions is first assessed by analyzing output from sixteen CMIP5 GCMs

under the “historical” forcing scenario. Figure 1 displays summer mean (May-October) rainfall and 850hPa winds based for observations and the GCM simulations. Observed summer mean rainfall (Fig. 1a) is largely characterized by an elongated rain belt along the ENP ITCZ near 10°N, extending into the North American monsoon (NAM) region along the Sierra Madre Occidental off the Gulf of California. A rainfall maximum center over northern South America is also present. In conjunction with this rainfall pattern, a prominent feature in the observed 850hPa wind fields over the ENP is the convergent flow onto the ITCZ, namely, the northeasterly winds to the north, and the southeasterly winds and cross-equatorial flow to the south of the ITCZ. It is noteworthy that very weak winds at 850hPa are largely observed over the far eastern portion of the ENP where the maximum summer rainfall resides, and even includes a westerly component. At the surface, southwesterly mean winds occur in the region of the warm pool precipitation maximum (not shown), a basic state flow that has been argued to be important for the dynamics of ISV in this region given its influence on the sign of flux anomalies for a given signed surface wind anomaly (e.g. Maloney and Esbensen 2007).

All the GCMs generally capture the bulk features of the ITCZ rain belt, the NAM, and rainfall over the South America, as well as associated 850hPa wind patterns. Note that daily 850hPa wind data based on historical simulations from CCSM4 and HadGEM2_ES were not available at the CMIP5 data portal at the time of analysis. Significant model deficiencies are also discernible. In several GCMs, the rainfall maximum along the ENP ITCZ is displaced to the west side of the ENP rather than the far eastern part of the ENP as in the observations, The models that display this bias include CCSM4, GFDL_ESM2M, INMCM4, two IPSL_CM5A GCMs, two MIROC_ESM GCMs, and Nor_ESM1_M. Meanwhile, the amplitude of mean rainfall, particularly over the coastal region near Central America, is

overestimated in several GCMs, which could be due in part to the relatively coarse resolutions in these GCMs that may create difficulties in resolving the fine-scale topographic features near the coast. While more objective evaluations of mean rainfall and 850hPa wind patterns in these GCMs will be illustrated in Fig. 2, it is worth mentioning that obvious deficiencies in simulated 850hPa zonal wind patterns over the ENP ITCZ along 10°N are apparent in Fig. 1 in many GCMs. In contrast to relatively weak easterly, or even westerly, winds at 850hPa over the ENP ITCZ in the observations as shown in Fig. 1a, strong easterly winds are detected in almost half of the sixteen GCMs analyzed. Table 2 illustrates the domain averaged summer mean zonal wind at 850hPa over the ENP ITCZ region (140°W-80°W; 5°N-25°N) in observations and the GCM simulations. As will be further illustrated below, the biases in representing the summer mean low-level winds over the ENP in a GCM appear to be closely linked to the model deficiencies in simulating local intraseasonal variability.

Figure 2 presents an objective assessment of the summer mean state simulated in each CMIP5 GCM by illustrating Taylor diagrams for rainfall and wind patterns over the ENP domain (150°W-80°W; 5°S-30°N). Taylor diagrams provide a way of quantifying how closely a simulated pattern matches its observational counterpart in terms of their pattern correlation, centered root-mean-square (RMS) difference, and the amplitude of their standard deviations (Taylor 2001). For rainfall patterns (Fig. 2a), while the two Had_GEM2 models (Had_GEM2_CC and Had_GEM2_ES) display the largest pattern correlations against the observations with correlation scores of about 0.93, the MRI_CGCM3 has the smallest RMS due to its better skill in simulating the spatial standard deviations of summer mean rainfall over the ENP. In addition, four other GCMs including CSIRO_mk3, MPI_ESM_LR, CanESM2, and CNRM_CM5 also exhibit relatively good pattern correlation scores

compared to other GCMs. Performance in simulating summer mean rainfall in a GCM is largely consistent with that for the circulation pattern at 850hPa. In general, models with relatively higher skill in simulating the summer mean rainfall pattern also exhibit better skill for the 850hPa wind pattern, particularly in the zonal wind component (Fig. 2b and 2c). Nevertheless, less defined stratification in model skill among the GCMs is found in simulated summer mean rainfall patterns than for winds.

Figure 3 illustrates the probability distribution function (PDF) of summer rainfall as a function of rainrate over the ENP ITCZ region (130-90°W; 5-15°N) based on both TRMM observations and GCM simulations. These PDFs were derived based on summertime (May-October) daily mean rainfall at each 2.5^{o}×2.5^{o} gridpoint during the periods of 1981-2005 and 1998-2010 for model simulations and observations, respectively. Results based on TRMM observations indicate that the largest frequency of daily mean rainfall occurs at 10 mm day^{-1} (Fig. 3a; note that rainrate on the x-axis in Fig. 3 is on a log scale). The frequency of occurrence markedly decreases when rainrate increases from 10 to 100 mm day^{-1}. In contrast, the decrease in the frequency is more gradual as rain rate decreases from 10 mm day^{-1} to very light rain. The frequency of occurrence peak at about 10mm day^{-1} as illustrated in TRMM is generally captured in most of the GCMs. Nevertheless, the observed rainfall PDF shape is reasonably well captured by only a very limited number of models, including HadGEM2_CC, HadGCM_ES, and MRI_CGCM3. Precipitation in most of the other GCMs tends to fall in a narrow rain-rate range centered at 10 mm day^{-1}. The observed frequency in both very heavy and light rainfall regimes is generally underestimated in these models. An extreme example is found in the INMCM4 (Fig. 3j), in which the rainfall over the ENP largely occurs in a range between 0.1 and 32 mm day^{-1}, in contrast to the much broader PDF in the observations. Also worth noting is that, in addition to a peak of 10 mm day^{-1}, modest

secondary frequency peaks are also discerned around the rain rate of 1 mm day^{-1} in the two HadGEM2 models (Figs. 3h and i). The causes of this bimodal distribution are not yet clear.

3.2 Intraseasonal Variability over the ENP

In this section, we proceed to examine how intraseasonal variability over the ENP is simulated in CMIP5 GCMs. Figure 4 illustrates general intraseasonal variability amplitude in both observations and CMIP5 GCM simulations by showing the standard deviations (STDs) of 10-90-day band-pass filtered summertime (May-October) rainfall in each dataset. In TRMM, intraseasonal variability in precipitation generally maximizes in regions of high mean precipitation (Figure 2), although intraseasonal variability is slightly displaced toward the Mexican coast relative to the mean precipitation distribution. ISV in the ENP is greatly underestimated in INMCM4 and two MIROC_ESM models. Relatively weak ISV amplitudes are also noticed in CanESM2, GFDL_ESM2M, and nor_ESM1. In contrast, too strong of ISV is simulated in the two HadGEM2 and two IPSL_CM5A GCMs. Meanwhile, maximum ISV activity is centered over the western part of the ENP in CCSM4, GFDL_ESM2M, INMCM4, two IPSL_CM5A GCMs, and Nor_ESM1_M, rather than over the eastern part of the ENP as in the observations. This analysis indicates that the ability of models to capture the overall level of intraseasonal variability in the east Pacific varies widely across models. In addition, the ability of models to simulate intraseasonal wind variance generally tracks their ability to simulate intraseasonal precipitation variance (not shown).

Next, in order to identify the leading ISV modes over the ENP in both observations and GCM simulations, complex empirical orthogonal function (CEOF) analysis was conducted for rainfall fields following the method of Maloney et al. (2008). In CEOF analysis, the covariance matrix is constructed from the complex analytic function at each grid point

consisting of the filtered time series of data plus *i* times its quadrature function, where the quadrature function is determined through a Hilbert transform. The resulting CEOFs are complex, and thus an advantage of CEOF analysis is that a propagating signal can be represented by one CEOF (Barnett 1983; Horel 1984; Maloney et al. 2008), rather than a quadrature pair of EOFs as in the traditional EOF approach or the extended EOF (EEOF) method as adopted by Jiang et al. (2011) to identify the two leading ENP ISV modes. Considering dominant influences of the 40-day ISV mode, as well as greater model uncertainty in representing the observed QBM over the ENP particularly in relatively coarse resolution GCMs as suggested by Jiang et al. (2011), in the present study we will focus on examining CMIP5 model fidelity in representing the 40-day ISV mode over the ENP. Prior to the CEOF analyses, daily rainfall fields based on both TRMM observations and GCM simulations are subject to 30-90-day band-pass filtering. CEOF analyses are then applied to daily rainfall anomalies from the model and observational datasets over the ENP domain (140°W-80°W; 5°N-25°N) during boreal summer (June-September).

Spatial patterns of the amplitude of the first CEOF mode (CEOF1) based on TRMM observations and GCM simulations are illustrated in Figure 5. Similarly to the behavior illustrated by Maloney et al. (2008), the maximum amplitude of the observed rainfall CEOF1 occurs over the far eastern part of the ENP (Fig. 5a). The spatial amplitude of the CEOF1 is rather weak in CanESM2, CCSM4, GFDL_ESM2M, INMCM4, two MIROC_ESM models, and Nor_ESM1_M, in general agreement with the weak amplitude in the STD patterns of 10-90-day band-pass filtered rainfall anomalies in these models shown in Fig. 4. A westward shift of the maximum amplitude relative to the observations is again evident in CCSM4, INMCM4, and the two IPSL_CM5A models. While the two HadGEM2 models well-capture the observed spatial distribution of the amplitude pattern, the CEOF1 amplitudes are stronger

than observed. The MPI_ESM_LR, CNRM_CM5, and CSIRO_Mk3 models produce approximately the correct amplitude and spatial distribution of the leading CEOF.

Figure 6 presents observed and GCM-simulated spatial phase patterns of the CEOF1 mode over the ENP. To make the spatial phase patterns of the CEOF1 based on the observations and simulations comparable to each other, the spatial phase of CEOF1 based on each dataset is adjusted by setting the domain averaged phase to be zero over a the region 110°W-100°W, 10-15°N. Contours of spatial patterns based on each dataset are only displayed where local variances explained by CEOF1 exceed 8%. Note that the direction of propagation associated with the CEOF1 is indicated by the gradient of the spatial phase. Figure 6a illustrates the spatial phase pattern of the observed rainfall CEOF1 after the phase adjustment. In accord with previous studies, the observed leading ISV mode over the ENP associated with the CEOF1 largely exhibits eastward propagation, although a northward component to propagation is also evident (e.g., Jiang and Waliser 2008; Maloney et al. 2008; Jiang et al. 2011).

The observed northeastward propagation associated with the leading ISV mode over the ENP as illustrated by the spatial phase pattern based on TRMM is reasonably well captured in several models, including CNRM_CM5, CSIRO_Mk3, GFDL_ESM2M, HadCM3, HadGEM2_CC, HadGEM2_ES, MPI_ESM_LR, and MRI_CGCM3, although the northward-propagating component in the two HadGEM2 models tends to dominate the eastward component. In contrast to the eastward propagation in the observations, westward propagation associated with CEOF1 is seen in several GCMs, including CanESM2, INMCM4, two IPSL_CM5A GCMs, and the two MIROC_ESM models.

The fidelity in simulating the leading ENP ISV mode by each CMIP5 model is then objectively assessed by calculating the pattern correlation of the simulated rainfall CEOF1

against its observed counterpart. To increase sampling when assessing the model skill scores, spatial patterns of rainfall anomalies associated with the CEOF1 based on both observations and GCM simulations are derived at two quadratic phases by multiplying the CEOF1 amplitude by the cosine and sine of the spatial phase on each grid point, respectively. Pattern correlations between the observed and simulated CEOF1 anomalous rainfall patterns over the ENP domain are then calculated at both of these two quadratic phases. A final pattern correlation score for a particular model in simulating the spatial pattern of the CEOF1 is derived by averaging these two pattern correlation coefficients. Figure 7 shows pattern correlation scores in depicting the CEOF1 rainfall pattern (x-axis) versus ENP domain averaged (5°-25°N; 140-80°W) CEOF1 amplitude relative to the observed counterpart (y-axis) in each model simulation. It is shown that a majority of the CMIP5 models tend to underestimate the amplitude of the leading ENP ISV mode associated with the rainfall CEOF1, except for CNRM_CM5, MPI_ESM_LR, and two versions of Had_GEM2. Also note that seven GCMs, including MRI_CGCM3, MPI_ESM_LR, CSIRO_Mk3, CNRM_CM5, and three versions of Hadley Center GCMs (i.e., Had_CM3, Had_GEM2_CC, Had_GEM2_ES) exhibit relatively high skill scores in capturing the CEOF1 patterns with correlation scores exceeding 0.75. Figure 7 succinctly illustrates that the CMIP5 models exhibit widely different ability to simulate intraseasonal variability in the ENP.

To show an example of how the spatial evolution associated with the leading ENP ISV modes are simulated in GCMs, Figure 8 illustrates the evolution of patterns of anomalous rainfall and 850hPa winds associated the ENP ISV in the observations and the five GCMs that exhibit relatively better pattern correlation scores in representing the observed CEOF1 as illustrated in Fig. 7. The evolution of anomalous rainfall and 850hPa winds in both observations and model simulations are derived by lag-regression against rainfall anomalies

averaged over a small domain over the ENP (110-100°W; 7.5-15°N; see the small red box in the top panel of Fig. 8a). Note that 30-90-day band-pass filtering was applied to all these fields prior to calculation of the regression patterns. In agreement with previous studies (e.g., Maloney and Esbensen 2007; Jiang and Waliser 2008; Jiang et al. 2011), Fig. 8a largely captures the main features of observed 40-day ISV mode over the ENP. An eastward-propagating signal that impinges from the west is clearly seen, which may be linked to the MJO over the Indian Ocean / Western Pacific. Enhanced convection over the ENP is found to be associated with anomalous low-level southwesterly winds. These prominent features of the observed leading ISV mode over the ENP are largely captured in these several GCMs that produce good intraseasonal simulations based on Figure 7.

It is noteworthy that the models with relatively better skill in representing the leading ENP ISV mode also tend to exhibit better skill at simulating summer mean rainfall and 850hPa wind patterns (c.f. Fig. 1 and Fig. 7). Further inspection of the summer mean 850hPa zonal wind (Table 2) illustrates that a common feature among these GCMs with relatively higher skill in simulating ENP ISV is the presence of westerly or very weak easterly mean winds (less than 1.5 m s^{-1}) over the ENP warm pool region, as in the observations. In contrast, most GCMs with relatively poor skill in simulating ISV exhibit a stronger easterly summer mean low-level flow (greater than 4 m s^{-1}). In Fig. 7, models with a westerly or very weak easterly summer mean 850hPa winds over the ENP are labeled with “square” marks, while those with strong easterly summer mean winds with “circle” marks. (Note that daily wind data were not available from the CMIP5 data portal at the time of this analysis for the two models with “diamond” marks.) A close association between summer mean 850hPa zonal wind and model performance in representing the leading ENP ISV mode is readily seen in Fig. 7. All the GCMs (except HadGEM2_ES due to missing wind data) that show pattern

correlation scores of greater than 0.75 are characterized by westerly or weak easterly summer mean winds at 850hPa. Therefore, these results strongly suggest that a realistic representation of the mean state could be conducive for improved simulations of the ENP ISV which has also been discussed for the MJO simulations over the western Pacific and Indian Ocean (e.g., Inness and Slingo 2003; Sperber et al. 2005; Kim et al. 2009; Kim et al. 2011).

One hypothesis for the close linkage between model performance in simulating the ISV and the low-level mean flow over the ENP is that a realistic mean state could produce the correct sign of surface flux anomalies relative to intraseasonal precipitation, which helps destabilize local intraseasonal disturbances (e.g. Maloney and Esbensen 2005; hereafter ME05). As seen in Fig. 8, the amplitude of anomalous southwesterly winds at 850hPa associated with enhanced convection of the leading ISV mode over the ENP is about 2 m s^{-1}. Therefore, under a westerly or weak easterly environmental summer mean flow, this anomalous southwesterly ISV wind will facilitate a positive feedback for the growth of ISV disturbances. Namely, stronger ISV convection over the ENP will lead to increased low-level southwesterly winds; this increased southwesterly low-level wind will further lead to enhanced surface latent heat fluxes (LHFX) under westerly or weak easterly flow, thus supporting tropospheric moisture anomalies and leading to intensification of ISV convection. However, with the presence of a strong mean easterly low-level wind, southwesterly anomalous wind in response to enhanced ISV convection will lead to a decrease of the total easterly winds, thus reducing LHFXs and dampening the existing ISV convective disturbances. Recently, Rydbeck et al. (2012) noted that easterly mean wind biases in a regional climate model were responsible for the inability of that model to sustain a local model intraseasonal variability over the east Pacific warm pool, creating the incorrect sign of

the latent heat flux anomalies relative to anomalous precipitation and column water vapor anomalies.

In order to substantiate the above hypothesis, we further analyze LHFX anomalies associated with the ISV over the ENP. Similar to Fig. 8, Figure 9 illustrates simultaneous regression patterns (i.e., day 0) of 30-90-day band-pass filtered LHFX (shaded) and 850hPa wind anomalies (vectors) against rainfall anomalies over the ENP box region based on both observations and GCM simulations. (Note that since results for the two versions of HadGEM2, IPSL_CM5A, and MIROC_ESM models greatly resemble each other, only results based on one version of these GCMs are presented in Fig. 9. Also, daily surface latent heat flux data were not available for CCSM4 and HadGCM3, and so results from these models are not shown in Fig. 9.) In agreement with previous findings by ME05, enhanced LHFX anomalies are found over convectively active regions of the ISV (c.f., Fig. 9a and Fig. 8a at day 0). Meanwhile, maximum positive latent heat flux anomalies tend to be collocated with the maximum anomalous wind speed (Fig. 9a), further suggesting the potentially critical role of anomalous wind to the surface LHFX anomalies as proposed by ME05. Thus, this configuration of anomalous surface wind, LHFX, and convection represents a positive feedback process to sustain the ENP ISV convection as previously described. These features are reasonably well simulated in CNRM_CM5, CSIRO_Mk3, HadGEM2_CC, MPI_ESM_LR, and MRI_CGCM3, consistent with relatively better skill in simulating ISV in these GCMs. Much stronger amplitudes in LHFX anomalies compared to observations are noted in CNRM_CM5 and HadGEM2_CC, in agreement with the stronger ISV convection and associated wind anomalies in these two models. On the other hand, anomalous LHFX patterns over the ENP simulated in several other GCMs are not as well organized as in the observations, including GFDL_ESM2M, INMCM4, IPSL_CM5A_LR, MIROC_ESM, and

nor_ESM1_M. As previously mentioned, these models are characterized by strong easterly summer mean flow at 850hPa over the ENP, and also exhibit poor skill in representing the ENP ISV in general. Taking INMCM4 as an example (Fig. 9g), although this model reasonably captures the low-level anomalous wind pattern corresponding to enhanced convection over the ENP (c.f., vectors in Fig. 9a and 9g), due to the presence of the easterly mean flow in the model, negative (positive) LHFX anomalies are found to be associated with westerly (easterly) wind anomalies. As a result, the strong negative LHFX anomalies over ISV convectively active regions will lead to a weakening of the initial ISV convection, thus providing a negative feedback to the ISV growth rate. While surface wind speed data are needed for an accurate diagnosis of the surface LHFX budget, the results presented in this part strongly suggest that a realistic mean flow in the model will greatly benefit its simulation of the ENP ISV through a realistic representation of the anomalous LHFX pattern and its feedback to ISV convection.

We cannot discount other reasons for why some models produce more realistic east Pacific intraseasonal variability than others, including improved convection parameterizations (e.g. Kim et al. 2009; Jiang et al. 2011); nor can we discount that the improved mean state is a result of improved intraseasonal variability that rectifies onto the low-level mean winds. However, our results at least strongly suggest an important role for a realistic depiction of low-level mean winds and their modulation of surface latent heat flux anomalies in producing more realistic intraseasonal variability in climate models, a result also supported by comparing the results of Small et al. (2011) and Rydbeck et al. (2012) in which the same regional coupled model run with different mean states is shown to produce substantially different east Pacific intraseasonal variability. We note no obvious relationship between horizontal resolution (Table 1) and the ability to produce realistic intraseasonal

variability. For example, CCSM4 is among one of the higher resolution models, but simulates variability very unrealistically; whereas HadCM3 is one of the coarsest, but produces one of the best variability simulations. This is largely in agreement with a previous study by Jiang et al. (2011), in which they demonstrated that GCM fidelity in simulating the 40-day ENP ISV mode seems not sensitive to model horizontal resolution, whereas increased resolution could be helpful for representing the QBM mode over the ENP.

4. Future Projection of the ISV over the ENP

In this section, future changes in characteristics of the ENP ISV are further explored by analyzing output from one model with relatively poor simulation of the ISV (CCSM4) and three models with relatively good ISV (HadGEM2_CC, HadGEM2_ES, MPI_ESM_LR) for the period of 2076-2099 under the RCP8.5 projection pathway.

Figure 10 illustrates projected changes in summer mean rainfall patterns over the ENP for the period of 2076-2100 under the RCP8.5 scenario relative to the present day climate (1981-2005) based on the four GCM simulations. Simulations based on these four GCMs exhibit good agreement with each other in that summertime precipitation is projected to be reduced in the northern part of the ENP warm pool and the Caribbean. Precipitation is projected to be enhanced over the southern part of the ENP between 5°N and 10°N, particularly in simulations based on CCSM4, HadGEM2_CC, HadGEM2_ES, suggesting a strengthening and southward shift of the ENP ITCZ. The positive rainfall change in MPI_ESM_LR is displaced slightly northward relative to that in the other three GCMs, and is also smaller in amplitude than both Hadley Center models. This projected change in summertime rainfall over the ENP and adjacent regions is generally in agreement with results derived based on a 15-member model ensemble as described in Part III of the overview paper the summarizes the NOAA CMIP5 Task Force's efforts in assessing the North American climate in CMIP5 models (Maloney and coauthors 2012). These results are also consistent

with changes in mean summertime precipitation in the east Pacific and Caribbean documented for CMIP3 models (e.g., Neelin et al. 2006).

Figure 11 further demonstrates projected changes in rain rate PDFs under the RCP8.5 scenario in the four GCMs. The background gray bars in each panel denote rainfall PDFs over the ENP during the period of 1981-2005, which are duplicated from Fig. 3, while green bars represent rainfall PDF changes in the future climate relative to that under the current climate (see axes on the right). Relative to today's climate, CCSM4 results suggest that fewer rain rate events of 10 mm day^{-1}, more rain rate events between 0.1 and 1 mm day^{-1}, and slightly more very heavy rainfall events (~ 100 mm day^{-1}) will occur in future climate. The other three GCMs (MPI_ESM_LR, HadGEM2_CC, HadGEM2_ES) project an increase in the frequency of heavy rain (> 10 mm day), and a decrease in occurrence of light rain. Recall that MPI_ESM_LR, HadGEM2_CC, and HadGEM2_ES produced better simulations of rainfall ISV in the current climate relative to CCSM4 (Section 3).

Next, we examine how ISV over the ENP changes in RCP8.5 based on the four aforementioned GCM simulations. Figure 12 illustrates differences in STD patterns of 10-90-day band-pass filtered rainfall between the two periods of 2076-2100 and 1981-2005. Largely mimicking the mean precipitation changes shown in Fig. 10, a significant increase in rainfall STD between 5°N and 10°N is noted in the ENP for all models. Significance is determined at the 95% confidence level using a Chi-squared test. Interestingly, some of these models also exhibit significant decreases in intraseasonal variability in the northern part of the ENP off the coast of Mexico/Central America and the Caribbean.

In Figure 13, we illustrate the spatial amplitude of the leading CEOF mode of summertime rainfall over the ENP simulated in the four GCMs for the period of 2076-2100. To facilitate the comparison, the spatial amplitude of CEOF1 derived from historical simulations in these four models is also shown in Fig. 13; the changes in the CEOF1 amplitude between the two periods are displayed in the lower panels. Largely consistent with

the projected changes in patterns of summer mean rainfall and the STD of 10-90-day filtered rainfall, amplitude increases of the leading CEOF are exhibited on the southern fringe of the original CEOF amplitude maximum in all four GCMs for the RCP8.5 scenario. Changes in the spatial phase of the leading CEOF mode among models are rather small, and thus are not shown here.

5. Summary

As one of the dominant forms of the tropical atmospheric variability, intraseasonal variability (ISV) over the eastern north Pacific (ENP) exerts pronounced influences on regional weather and climate, and hence provides a primary source for extended range climate prediction. Moreover, as GCMs have become essential tools for prediction and projections of future climate, current model deficiencies in representing this fundamental component of atmospheric variability leave us greatly disadvantaged in climate change studies. As a part of collective efforts coordinated by the NOAA MAPP program's CMIP5 Task Force to assess North American climate simulated in CMIP5 models, we have evaluated model fidelity at representing ENP ISV in sixteen GCMs participating in the CMIP5 project. Among the sixteen CMIP5 GCMs examined in this study, only seven GCMs capture the spatial pattern of the leading ISV mode over the ENP reasonably well, although even these several GCMs exhibit biases in simulating ISV amplitude.

Analyses further indicate that model fidelity in representing the ENP ISV in a GCM is closely associated with its ability to simulate a realistic summer mean state. The presence of a westerly or very weak easterly low-level mean wind over the ENP warm pool region in a model, as in the observations, appears conducive to more realistic simulation of east Pacific ISV. One hypothesis is that a realistic mean state could produce the correct sign of surface flux anomalies relative to the ISV convection, which helps to destabilize local intraseasonal disturbances through a positive feedback between convection and wind-induced surface

latent heat fluxes as proposed by Maloney and Esbensen (2005). When strong easterly mean low-level flow is present over the ENP in the biased models, southwesterly wind anomalies in response to the enhanced convection will lead to local negative latent heat flux anomalies, thus weakening the existing ISV disturbances. This hypothesis does not rule out other reasons for better variability in some models, such as improved parameterizations of deep convection.

Projected changes in the characteristics of ENP ISV under the RCP8.5 projection pathway are also explored in simulations from four CMIP5 GCMs. Consistent with the future change in the summer mean rainfall pattern, analyses based on these four CMIP5 models project that the amplitude of ISV will be enhanced over the southern part of the ENP between 5°N and 10°N, while reduced over the northern ENP off the coastal region of Mexico / Central America and the Caribbean.

Acknowledgments*:* The authors acknowledge the support of NOAA Climate Program Office Modeling, Analysis, Predictions and Projections (MAPP) Program as part of the CMIP5 Task Force. Work was supported under grant NA09OAR4310191 and NA11OAR4310086 (XJ) and NA08OAR4320893 #7 and #14 (EDM). We also acknowledge support from the NSF Climate and Large-Scale Dynamics Program under Award ATM-0934285 (XJ), AGS-0946911, and AGS-1025584 (EDM). Part of this research was carried out at the Jet Propulsion Laboratory, California Institute of Technology, under a contract with the National Aeronautics and Space Administration. Global ocean heat flux and evaporation products were provided by the WHOI OAFlux project (http://oaflux.whoi.edu)

References

Barnett, T. P., 1983: Interaction of the Monsoon and Pacific Trade-Wind System at Interannual Time Scales .1. The Equatorial Zone. *Mon. Weather Rev.*, **111,** 756-773.

Chou, S.-H., E. J. Nelkin, J. Ardizzone, R. Atlas, and C. L. Shie, 2001: Goddard Satellite-based Surface Turbulent Fluxes (GSSTF) - Version 2 Documentation. Distributed Active Archive Center (DAAC), NASA Goddard Space Flight Center, Greenbelt, Maryland., .

Dee, D. P., et al., 2011: The ERA-Interim reanalysis: configuration and performance of the data assimilation system. *Quart. J. Roy. Meteor. Soc.*, **137**, 10.1002/qj.828**,** 553-597.

Higgins, R. W. and W. Shi, 2001: Intercomparison of the Principal Modes of Interannual and Intraseasonal Variability of the North American Monsoon System. *J. Clim.*, **14,** 403-417.

Horel, J. D., 1984: Complex Principal Component Analysis - Theory and Examples. *Journal of Climate and Applied Meteorology*, **23,** 1660-1673.

Huffman, G. J., R. F. Adler, B. Rudolf, U. Schneider, and P. R. Keehn, 1995: Global Precipitation Estimates Based on a Technique for Combining Satellite-Based Estimates, Rain-Gauge Analysis, and Nwp Model Precipitation Information. *J. Clim.*, **8,** 1284-1295.

Inness, P. M. and J. M. Slingo, 2003: Simulation of the Madden-Julian oscillation in a coupled general circulation model. Part I: Comparison with observations and an atmosphere-only GCM. *J. Clim.*, **16,** 345-364.

Jiang, X. and D. E. Waliser, 2008: Northward propagation of the subseasonal variability over the eastern Pacific warm pool. *Geophys. Res. Lett.*, **35**, L09814, doi:10.1029/2008GL033723.

——, 2009: Two dominant subseasonal variability modes of the eastern Pacific ITCZ. *Geophys. Res. Lett.*, **36**, L04704, doi: 10.1029/2008gl036820.

Jiang, X., T. Li, and B. Wang, 2004: Structures and Mechanisms of the Northward Propagating Boreal Summer Intraseasonal Oscillation. *J. Clim.*, **17,** 1022-1039.

Jiang, X., D. Waliser, D. Kim, M. Zhao, K. Sperber, W. Stern, S. Schubert, G. Zhang, W. Wang, M. Khairoutdinov, R. Neale, and M.-I. Lee, 2011: Simulation of the

intraseasonal variability over the Eastern Pacific ITCZ in climate models. *Climate Dyn.*, 10.1007/s00382-011-1098-x**,** 1-20.

Kim, D., A. H. Sobel, E. D. Maloney, D. M. W. Frierson, and I. S. Kang, 2011: A Systematic Relationship between Intraseasonal Variability and Mean State Bias in AGCM Simulations. *J. Clim.*, **24**, Doi 10.1175/2011jcli4177.1**,** 5506-5520.

Kim, D., et al., 2009: Application of MJO Simulation Diagnostics to Climate Models. *J. Clim.*, **22**, Doi 10.1175/2009jcli3063.1**,** 6413-6436.

Lin, J.-L., et al., 2006: Tropical Intraseasonal Variability in 14 IPCC AR4 Climate Models. Part I: Convective Signals. *J. Clim.*, **19,** 2665-2690.

Lorenz, D. J. and D. L. Hartmann, 2006: The Effect of the MJO on the North American Monsoon. *J. Clim.*, **19,** 333-343.

Madden, R. A. and P. R. Julian, 1994: Observations of the 40-50-Day Tropical Oscillation: A Review. *Mon. Weather Rev.*, **122,** 814-837.

Magana, V., J. A. Amador, and S. Medina, 1999: The midsummer drought over Mexico and Central America. *J. Clim.*, **12,** 1577-1588.

Maloney, E. D. and D. L. Hartmann, 2000a: Modulation of Eastern North Pacific Hurricanes by the Madden-Julian Oscillation. *J. Clim.*, **13,** 1451-1460.

——, 2000b: Modulation of hurricane activity in the Gulf of Mexico by the Madden-Julian oscillation. *Science*, **287,** 2002-2004.

Maloney, E. D. and S. K. Esbensen, 2003: The Amplification of East Pacific Madden-Julian Oscillation Convection and Wind Anomalies during June-November. *J. Clim.*, **16,** 3482-3497.

Maloney, E. D. and S. K. Esbensen, 2005: A Modeling Study of Summertime East Pacific Wind-Induced Ocean-Atmosphere Exchange in the Intraseasonal Oscillation. *J. Clim.*, **18,** 568-584.

——, 2007: Satellite and Buoy Observations of Boreal Summer Intraseasonal Variability in the Tropical Northeast Pacific. *Mon. Weather Rev.*, **135,** 3-19.

Maloney, E. D. and coauthors, 2012: North American Climate in CMIP5 Experiments: Part III: Assessment of 21st Century Projections. *J. Clim.***,** submitted.

Maloney, E. D., D. B. Chelton, and S. K. Esbensen, 2008: Subseasonal SST variability in the tropical eastern north Pacific during boreal summer. *J. Clim.*, **21**, Doi 10.1175/2007jcli1856.1**,** 4149-4167.

Martin, E. R. and C. Schumacher, 2010: Modulation of Caribbean Precipitation by the Madden-Julian Oscillation. *J. Clim.*, doi:10.1175/2010JCLI3773.1**,** in press.

Neelin, J. D., M. Munnich, H. Su, J. E. Meyerson, and C. E. Holloway, 2006: Tropical drying trends in global warming models and observations. *Proc. Natl. Acad. Sci.*, **103**, DOI 10.1073/pnas.0601798103**,** 6110-6115.

Reynolds, R. W., T. M. Smith, C. Liu, D. B. Chelton, K. S. Casey, and M. G. Schlax, 2007: Daily High-Resolution-Blended Analyses for Sea Surface Temperature. *J. Clim.*, **20**, 10.1175/2007jcli1824.1**,** 5473-5496.

Rydbeck, A. V., E. D. Maloney, S.-P. Xie, J. Hafner, and J. Shaman, 2012: Remote Forcing Versus Local Feedback of East Pacific Intraseasonal Variability. *J. Clim.***,** in press.

Serra, Y. L., G. N. Kiladis, and K. I. Hodges, 2010: Tracking and Mean Structure of Easterly Waves over the Intra-Americas Sea. *J. Clim.*, **23**, doi:10.1175/2010JCLI3223.1**,** 4823-4840.

Slingo, J. M., et al., 1996: Intraseasonal oscillations in 15 atmospheric general circulation models: Results from an AMIP diagnostic subproject. *Climate Dyn.*, **12,** 325-357.

Small, R. J., S. P. De Szoeke, and S.-P. Xie, 2007: The Central American midsummer drought: Regional aspects and large-scale forcing. *J. Clim.*, **20**, Doi 10.1175/Jcli4261.1**,** 4853-4873.

Small, R. J., S. P. Xie, E. D. Maloney, S. P. de Szoeke, and T. Miyama, 2011: Intraseasonal variability in the far-east pacific: investigation of the role of air-sea coupling in a regional coupled model. *Climate Dyn.*, **36**, DOI 10.1007/s00382-010-0786-2**,** 867-890.

Sperber, K. R., S. Gualdi, S. Legutke, and V. Gayler, 2005: The Madden-Julian oscillation in ECHAM4 coupled and uncoupled general circulation models. *Climate Dyn.*, **25**, DOI 10.1007/s00382-005-0026-3**,** 117-140.

Taylor, K. E., 2001: Summarizing multiple aspects of model performance in a single diagram. *J. Geophys. Res.*, **106,** 7183-7192.

Taylor, K. E., R. J. Stouffer, and G. A. Meehl, 2012: An Overview of Cmip5 and the Experiment Design. *Bull. Am. Meteorol. Soc.*, **93**, Doi 10.1175/Bams-D-11-00094.1**,** 485-498.

Waliser, D. E., 2011: Predictability and Forecasting. *Intraseasonal Variability in the Atmosphere-Ocean Climate System*, Second ed. W. K. M. Lau and D. E. Waliser, Eds., Springer, Heidelberg, Germany, In Press.

Waliser, D. E., et al., 2003: AGCM simulations of intraseasonal variability associated with the Asian summer monsoon. *Climate Dyn.*, **21**, DOI 10.1007/s00382-003-0337-1**,** 423-446.

Wu, M. L. C., S. D. Schubert, M. J. Suarez, and N. E. Huang, 2009: An Analysis of Moisture Fluxes into the Gulf of California. *J. Clim.*, **22**, Doi 10.1175/2008jcli2525.1**,** 2216-2239.

Yu, L., X. Jin, and R. A. Weller, 2008: Multidecade Global Flux Datasets from the Objectively Analyzed Air-sea Fluxes (OAFlux) Project: Latent and sensible heat fluxes, ocean evaporation, and related surface meteorological variables. Woods Hole Oceanographic Institution, OAFlux Project Technical Report. OA-2008-01, 64pp., Woods Hole. Massachusetts, .

List of Tables

Table 1 CMIP5 models analyzed in this study.

Table 2 Summer mean zonal wind speed at 850hPa over the ENP (140°W-80°W; 5°N-25°N; unit: m s^{-1}) in observations and GCM simulations

List of Figures

Figure 1 Observed and simulated summer mean (May–October) rainfall patterns (shaded; see color bar at the bottom) and 850hPa winds (vectors; m s^{-1}). Observed rainfall and winds are based on TRMM and ERA-I reanalysis for the period of 1998-2010, while model mean state is derived from historical simulations based on GCMs for the period of 1981-2005.

Figure 2 Taylor diagrams for summer mean (May-September) (a) precipitation, (b) 850hPa u-wind, (c) 850hPa v-wind over the ENP (150°W-80°W; 5°S-30°N) simulated in CMIP5 GCMs.

Figure 3 The probability distribution function (PDF) of summer rainfall over the ENP (130-90°W; 5-15°N) as a function of rainrate based on observations and GCM simulations. The observed PDF is also duplicated in panels (b)-(q) with purple lines. The rainrate on the x-axis is plotted on a log scale.

Figure 4 Standard deviations of 10-90-day band-pass filtered summertime (May–September) rainfall based on observations and CMIP5 model simulations (unit: mm day^{-1}).

Figure 5 Spatial distribution of amplitude of the CEOF1 mode of 30-90-day band-pass filtered rainfall during boreal summer (June-September) over the ENP based on observations and model simulations.

Figure 6 Same as in Fig. 5, but for spatial distribution of phase of the summertime rainfall CEOF1 mode over the ENP. The spatial phase based on each dataset is adjusted by setting the domain averaged value to be zero over the box region of 110°W-100°W, 10-15°N. Contours are only displayed over grids with local variances explained by CEOF1 exceeding 8%.

Figure 7 X-axis: Pattern correlation coefficients of the CEOF1 mode between TRMM observations and CMIP5 GCM simulations. Y-axis: Relative amplitudes of CEOF1 in model simulations to the observed counterpart. Both pattern correlations and

amplitudes are derived by averaging over the area of 5°N-25°N, 140°W-80°W where the active ISV is observed. The black "star" mark represents the TRMM observations. Models with "square" marks display westerly or weak easterly (<1.5 m s^{-1}) summer mean wind at 850hPa, while strong easterly winds (> 4 m s^{-1}) are noted in models with "circle" marks. Wind fields are not available in the data portal at the time of this analysis from the two GCMs with "diamond" marks.

Figure 8 Evolution of anomalous rainfall (shaded) and 850hPa winds (vectors) associated with the dominant ISV mode over the ENP as derived by lag-regressions against the corresponding rainfall anomalies over 100-110°W; 7.5^{o}N-15°N (see the red box in the upper left panel) based on observations and CMIP5 model simulations.

Figure 9 Simultaneous regression patterns (e.g., day 0) of anomalous surface latent heat flux (shaded) and 850hPa winds (vectors) against the corresponding rainfall anomalies over the ENP box (100-110°W; 7.5^{o}N-15°N) in observations and model simulations.

Figure 10 Projected changes in summer mean rainfall patterns between the period of 2076-2099 under RCP 8.5 scenario and 1981-2005 based on historical simulations.

Figure 11 (Grey shading with left axes): The PDF of summer rainfall as a function of rain rate over the ENP (130-90°W; 5-15°N) based on historical (1981-2005) from four GCMs - CCSM4, Had_GEM2_CC, Has_GEM2_ES, and MPI_ESM_LR (reproduced from Fig. 3). (Green shading with right axes): Changes in rainfall PDFs in future projections (2076-2099) under the RCP8.5 projection scenario. The precipitation rate on x-axis is plotted on a log scale.

Figure 12 Difference in the standard deviation of the 10-90 day bandpass filtered precipitation in the CCSM4, MPI_ESM, HAD_GEM2_CC, and HAD_GEM_ES models. Units are mm day^{-1}. Stippling shows where the variance difference is significantly different from zero at the 95% confidence level using a Chi-squared test.

Figure 13 Spatial distributions of CEOF1 amplitude of summer rainfall over the ENP based on four CMIP5 models in historical simulations (upper panels) and future projections under the RCP 8.5 scenario (middle panels) and their differences (lower panels)

Table 1. CMIP5 models analyzed in this study.

Model Name	**Modeling Center**	**Horizontal Resolution of Atmospheric Model** (lon × lat deg)	**Scenario**
CanESM2	Canadian Center for Climate Modeling and Analysis	2.8 × 2.8	"historical"
CCSM4	US National Center for Atmospheric Research	1.25 × 1	"historical" , "RCP8.5"
CNRM-CM5	National Centre for Meteorological Research, France	1.4 × 1.4	"historical"
CSIRO-MK3	Commonwealth Scientific and Industrial Research Organization /Queensland Climate Change Centre of Excellence, AUS	1.8 × 1.8	"historical"
GFDL-ESM2M	NOAA Geophysical Fluid Dynamics Laboratory	2.5 × 2.0	"historical"
HadCM3 HadGEM2-CC HadGEM2-ES	UK Met Office Hadley Centre	3.7 × 2.5 1.8 × 1.25 1.8 × 1.25	"historical" "historical", "RCP8.5" "historical", "RCP8.5"
INMCM4	Institute for Numerical Mathematics, Russia	2 × 1.5	"historical"
IPSL-CM5A-LR IPSL-CM5A-MR	Institute Pierre Simon Laplace, France	3.75 × 1.8 2.5 × 1.25	"historical"
MIROC-ESM MIROC-ESM-CHEM	Atmosphere and Ocean Research Institute (The University of Tokyo), National Institute for Environmental Studies, and Japan Agency for Marine-Earth Science and Technology, Japan	1.4 × 1.4	"historical"
MPI-ESM-LR	Max Planch Institute for Meteorology, Germany	1.9 × 1.9	"historical", "RCP8.5"
MRI-CGCM3	Meteorological Research Institute, Japan	1.1 × 1.1	"historical"
NorESM1-M	Norwegian Climate Center, Norway	2.5 × 1.9	"historical"

Table 2 Summer mean zonal wind speed at 850hPa over the ENP (140°W-80°W; 5°N-25°N; unit: m s^{-1}) in observations and GCM simulations

OBS	CanESM2	CCSM4	CNRM_CM5	CSIRO_Mk3	GFDL_ESM2M	HadCM3	HadGEM2_CC	HadGEM2_ES
0.63	-4.02	n/a	-0.77	1.11	-4.2	-0.6	0.2	n/a
	INMCM4	IPSL_CM5A_LR	IPSL_CM5A_MR	MIROC_ESM	MIROC_ESM_CHEM	MPI_ESM_LR	MRI_CGCM3	Nor_ESM1_M
	-6.5	-6.1	-6.6	-6.4	-5.9	0.42	-1.45	-9.2

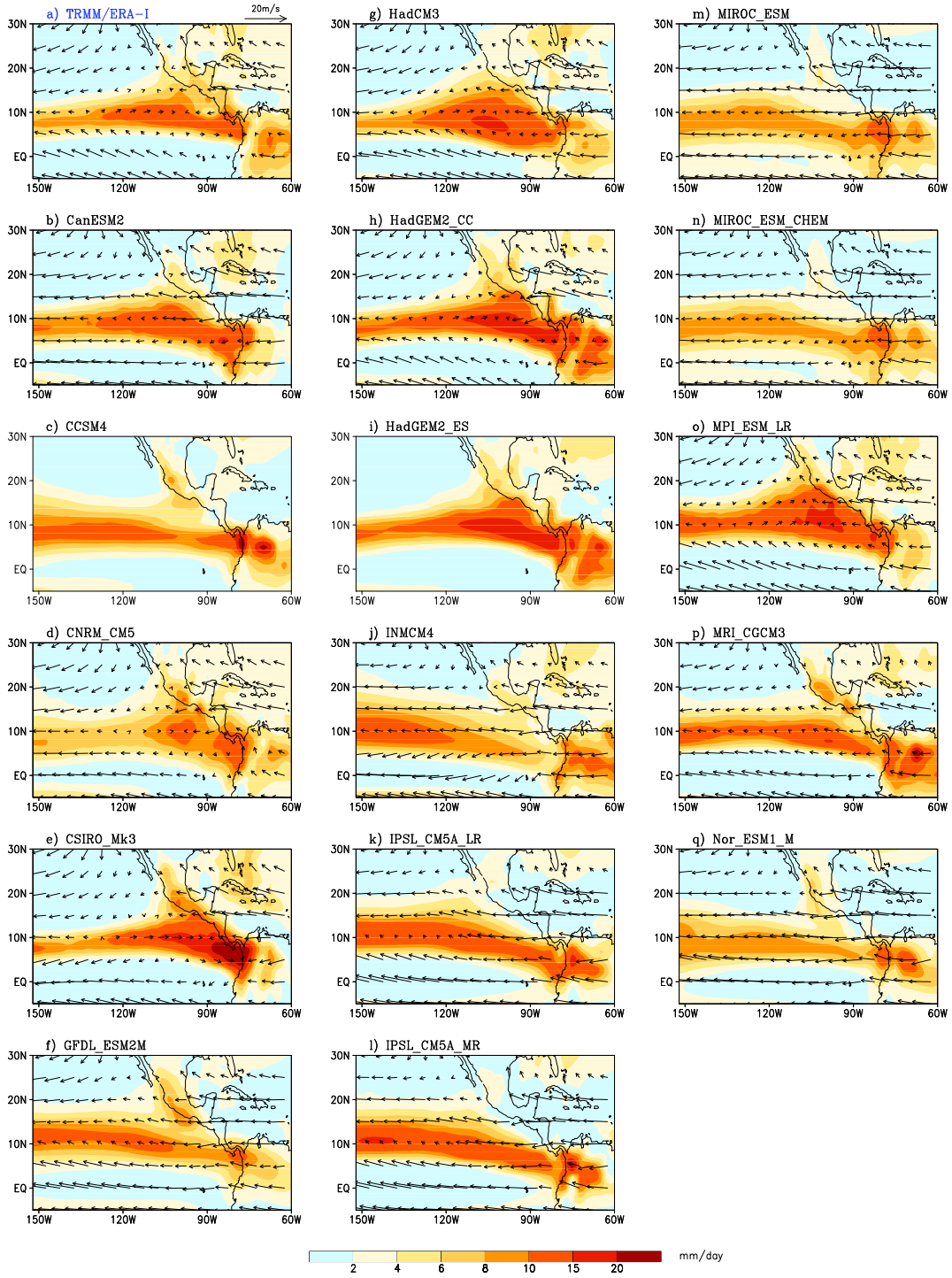

Figure 1 Observed and simulated summer mean (May–October) rainfall patterns (shaded; see color bar at the bottom) and 850hPa winds (vectors; m s^{-1}). Observed rainfall and winds are based on TRMM and ERA-I reanalysis for the period of 1998-2010, while model mean state is derived from historical simulations based on GCMs for the period of 1981-2005.

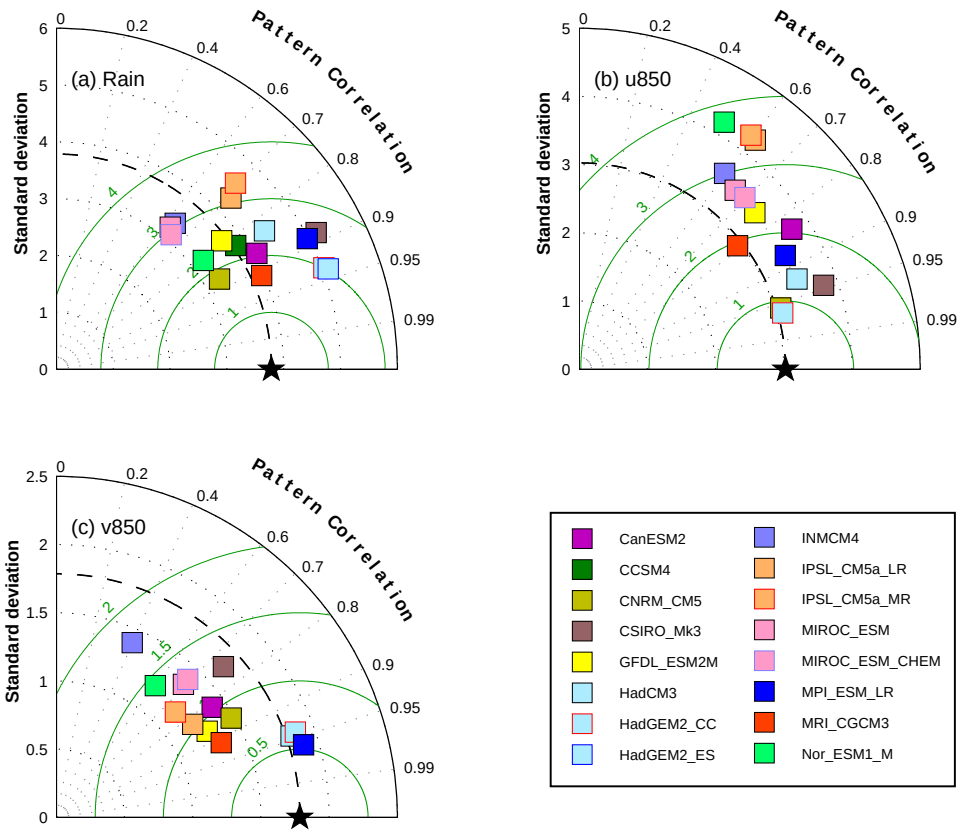

Figure 2 Taylor diagrams for summer mean (May-September) (a) precipitation, (b) 850hPa u-wind, (c) 850hPa v-wind over the ENP (150°W-80°W; 5°S-30°N) simulated in CMIP5 GCMs.

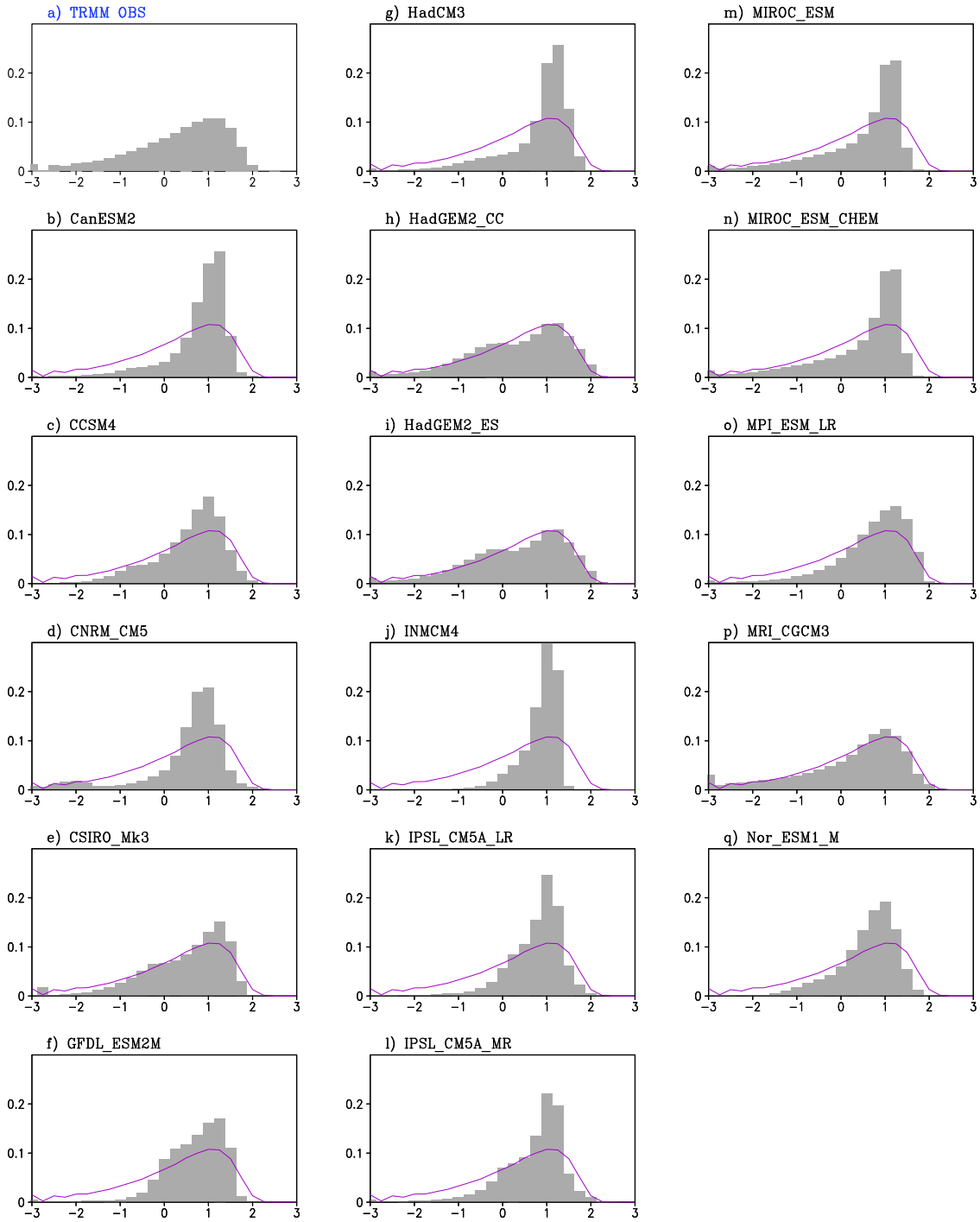

Figure 3 Grey bars: The probability distribution function (PDF) of summer rainfall over the ENP (130-90°W; 5-15°N) as a function of rainrate based on observations and GCM simulations. The observed PDF is also duplicated in panels (b)-(q) with purple lines. The rainrate on the x-axis is plotted on a log scale.

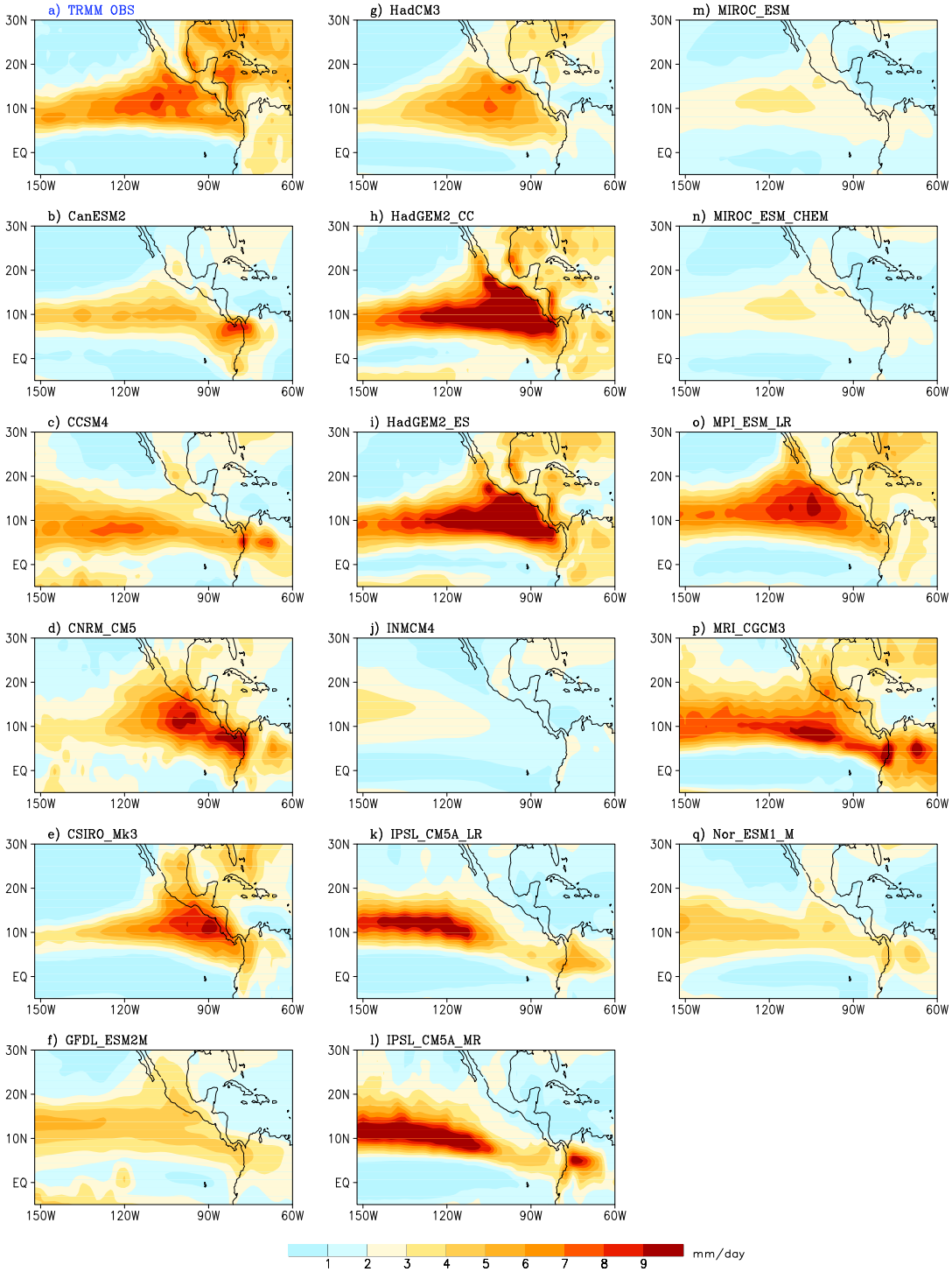

Figure 4 Standard deviations of 10-90-day band-pass filtered summertime (May–September) rainfall based on observations and CMIP5 model simulations (unit: mm day^{-1}).

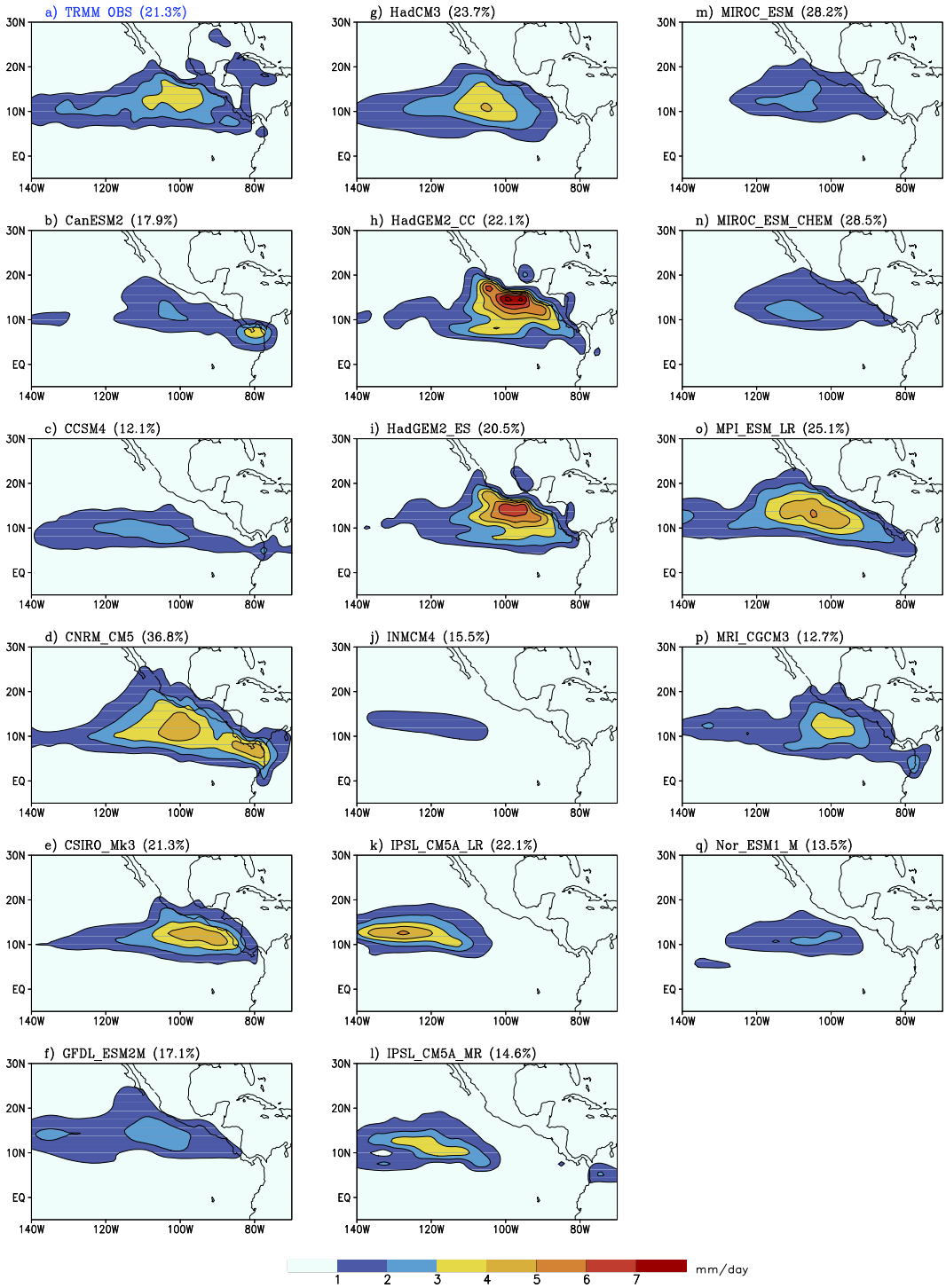

Figure 5 Spatial distribution of amplitude of the CEOF1 mode of 30-90-day band-pass filtered rainfall during boreal summer (June-September) over the ENP based on observations and model simulations.

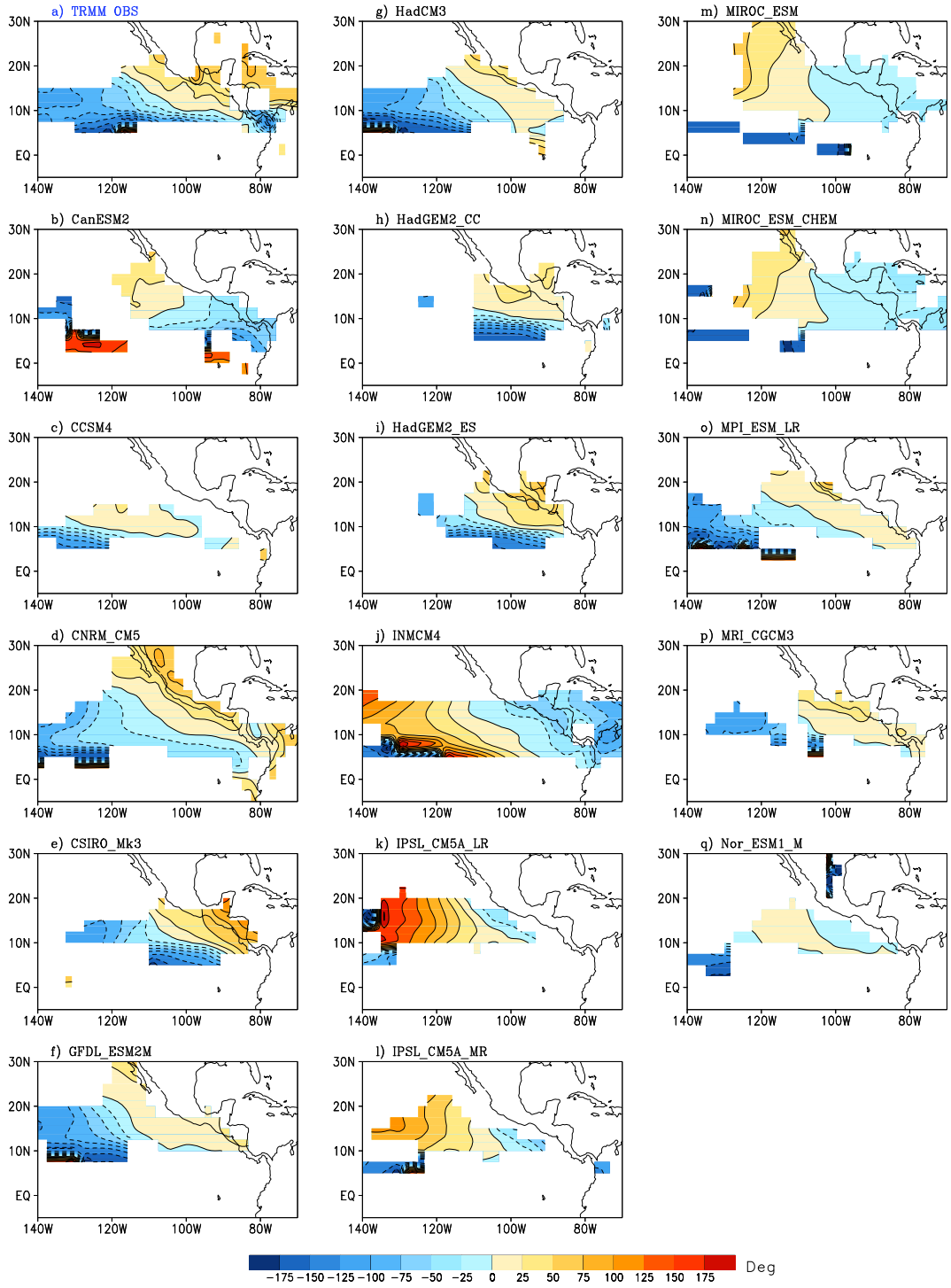

Figure 6 Same as in Fig. 5, but for spatial distribution of phase of the summertime rainfall CEOF1 mode over the ENP. The spatial phase based on each dataset is adjusted by setting the domain averaged value to be zero over the box region of 110°W-100°W, 10-15°N. Contours are only displayed over grids with local variances explained by CEOF1 exceeding 8%.

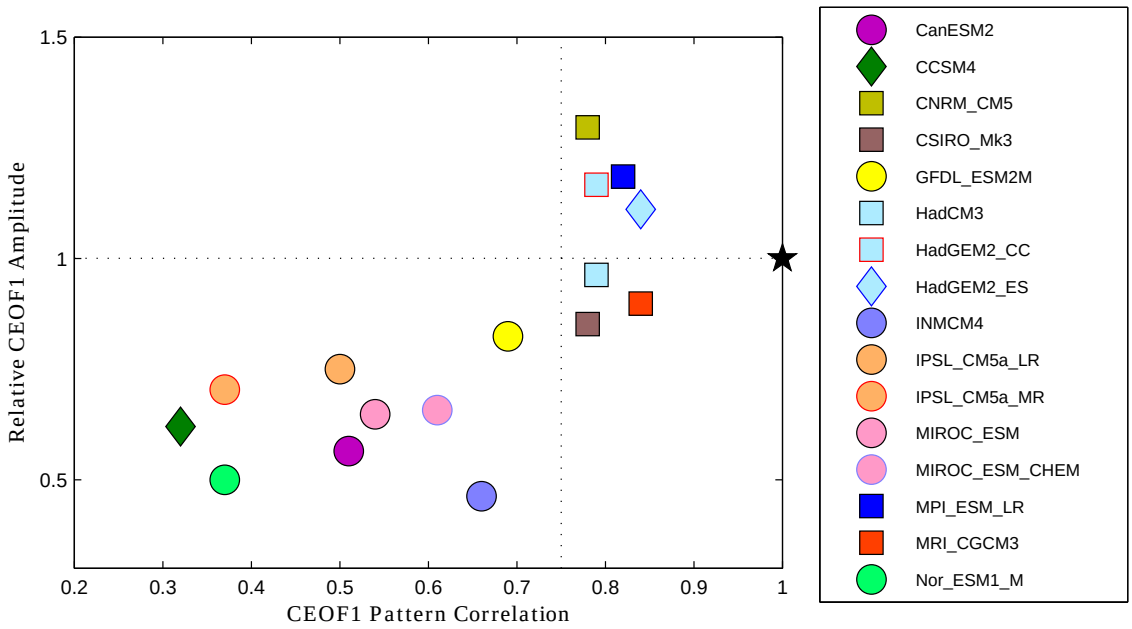

Figure 7 X-axis: Pattern correlation coefficients of the CEOF1 mode between TRMM observations and CMIP5 GCM simulations. Y-axis: Relative amplitudes of CEOF1 in model simulations to the observed counterpart. Both pattern correlations and amplitudes are derived by averaging over the area of 5°N-25°N, 140°W-80°W where the active ISV is observed. The black "star" mark represents the TRMM observations. Models with "square" marks display westerly or weak easterly (<1.5 m s^{-1}) summer mean wind at 850hPa, while strong easterly winds (> 4 m s^{-1}) are noted in models with "circle" marks. Wind fields are not available in the data portal at the time of this analysis from the two GCMs with "diamond" marks.

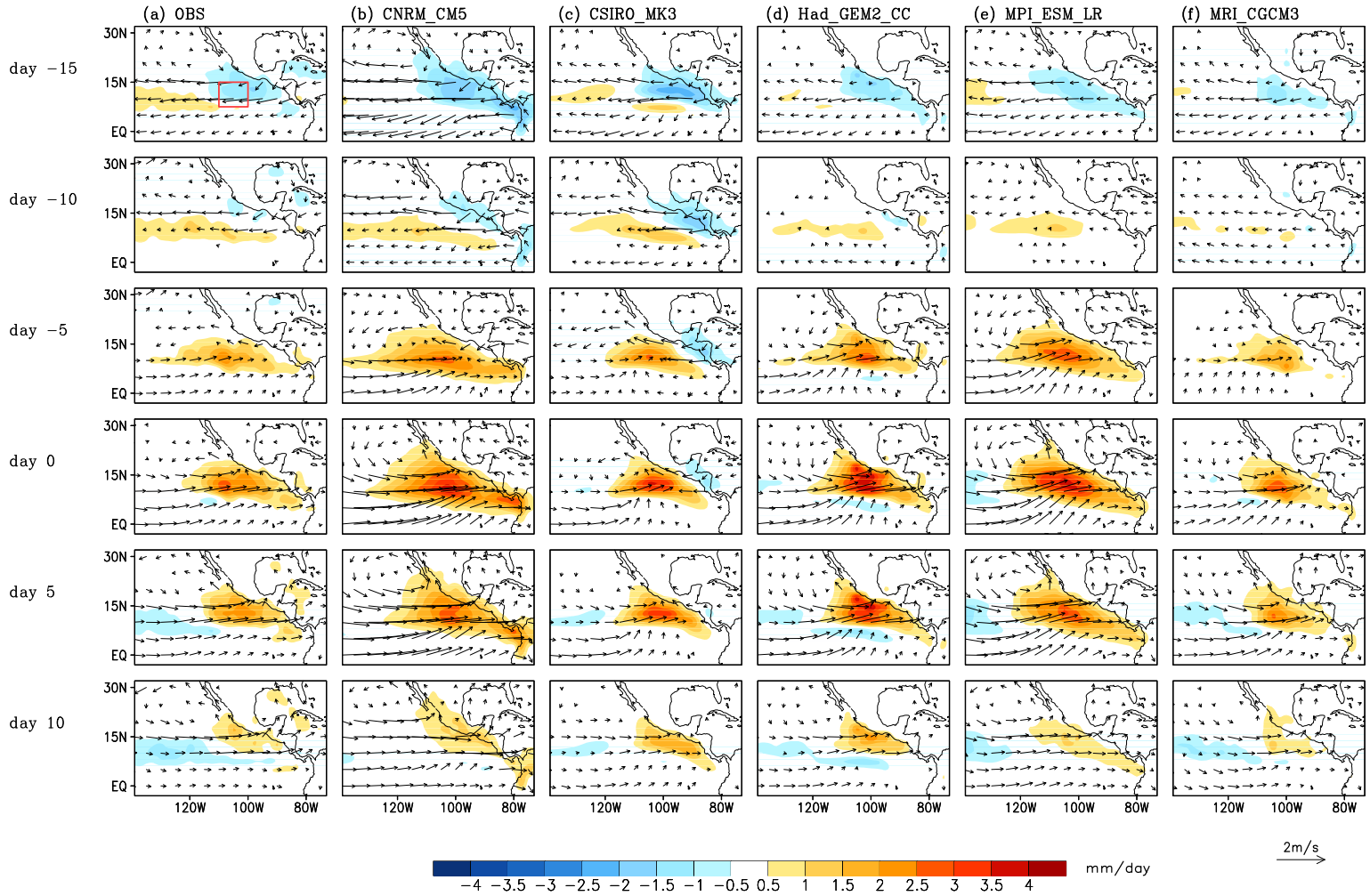

Figure 8 Evolution of anomalous rainfall (shaded) and 850hPa winds (vectors) associated with the dominant ISV mode over the ENP as derived by lag-regressions against the corresponding rainfall anomalies over 100-110°W; 7.5°N-15°N (see the red box in the upper left panel) based on observations and CMIP5 model simulations.

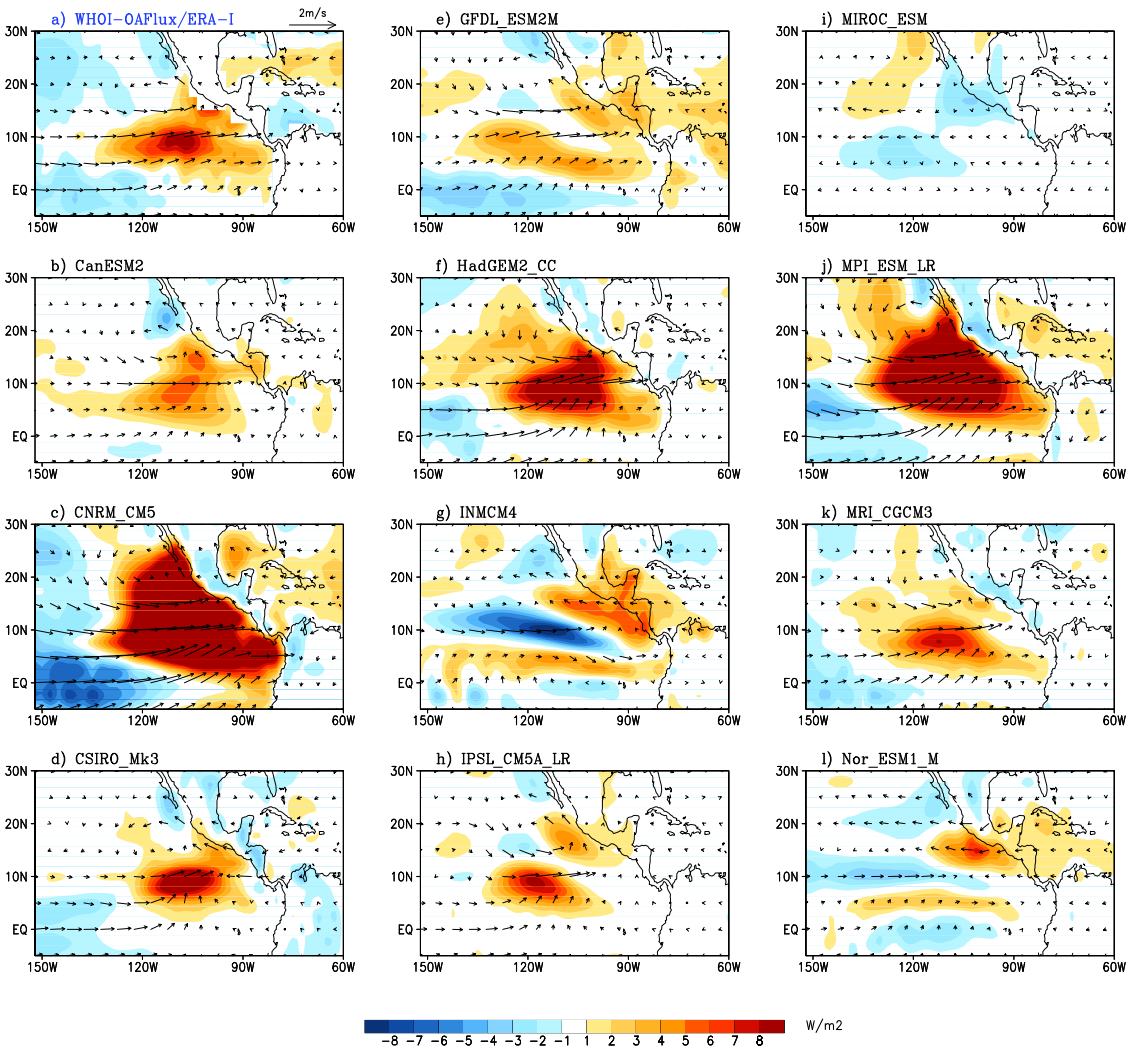

Figure 9 Simultaneous regression patterns (e.g., day 0) of anomalous surface latent heat flux (shaded) and 850hPa winds (vectors) against the corresponding rainfall anomalies over the ENP box (100-110°W; 7.5^{o}N-15°N) in observations and model simulations.

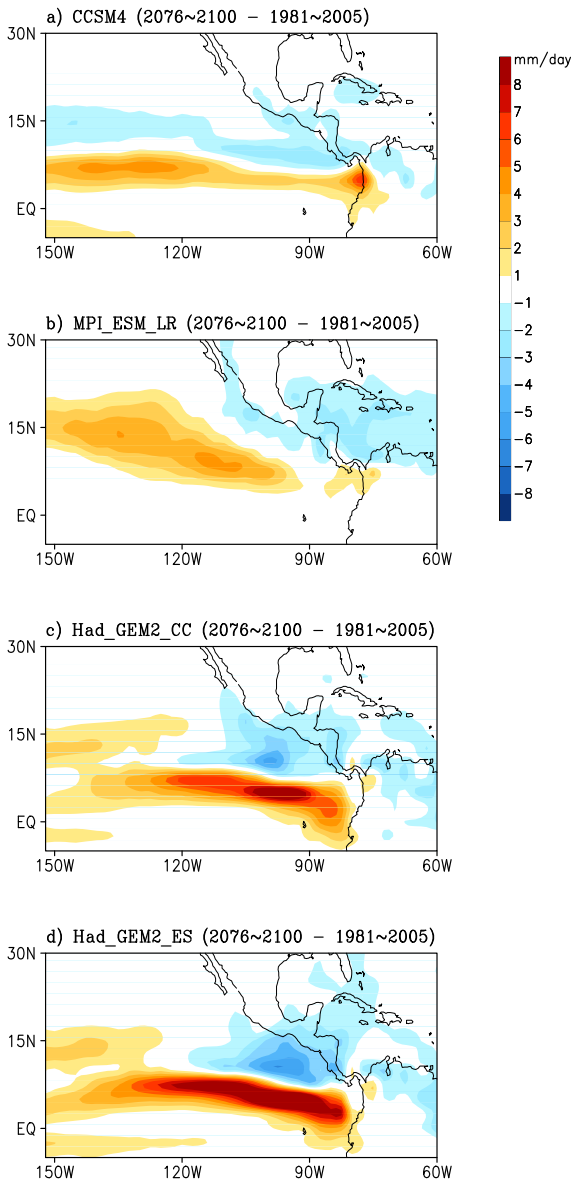

Figure 10 Projected changes in summer mean rainfall patterns between the period of 2076-2099 under the RCP 8.5 projection scenario and 1981-2005 based on historical simulations.

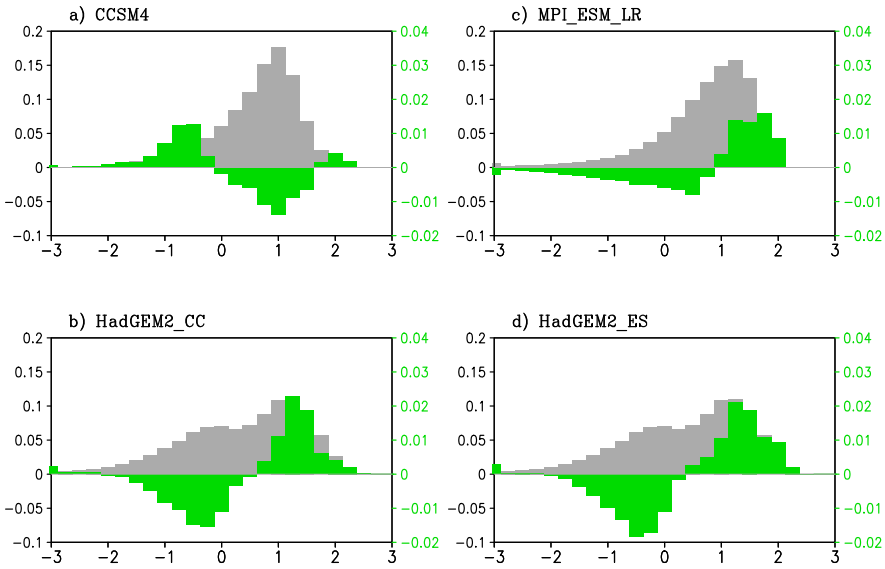

Figure 11 (Grey shading with left axes): The PDF of summer rainfall as a function of rain rate over the ENP (130-90°W; 5-15°N) based on historical (1981-2005) from four GCMs - CCSM4, Had_GEM2_CC, Has_GEM2_ES, and MPI_ESM_LR (reproduced from Fig. 3). (Green shading with right axes): Changes in rainfall PDFs in future projections (2076-2099) under the RCP8.5 projection scenario. The precipitation rate on x-axis is plotted on a log scale.

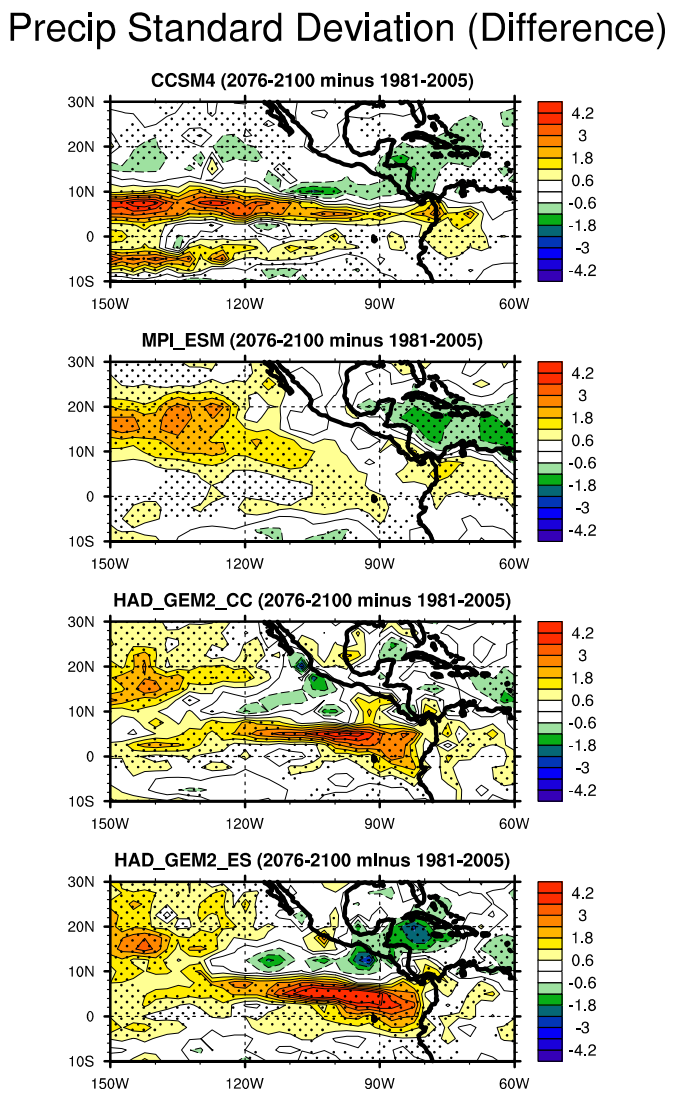

Figure 12 Difference in the standard deviation of the 10-90 day bandpass filtered precipitation in the CCSM4, MPI_ESM, HAD_GEM2_CC, and HAD_GEM_ES models. Units are mm day^{-1}. Stippling shows where the variance difference is significantly different from zero at the 95% confidence level using a Chi-squared test.

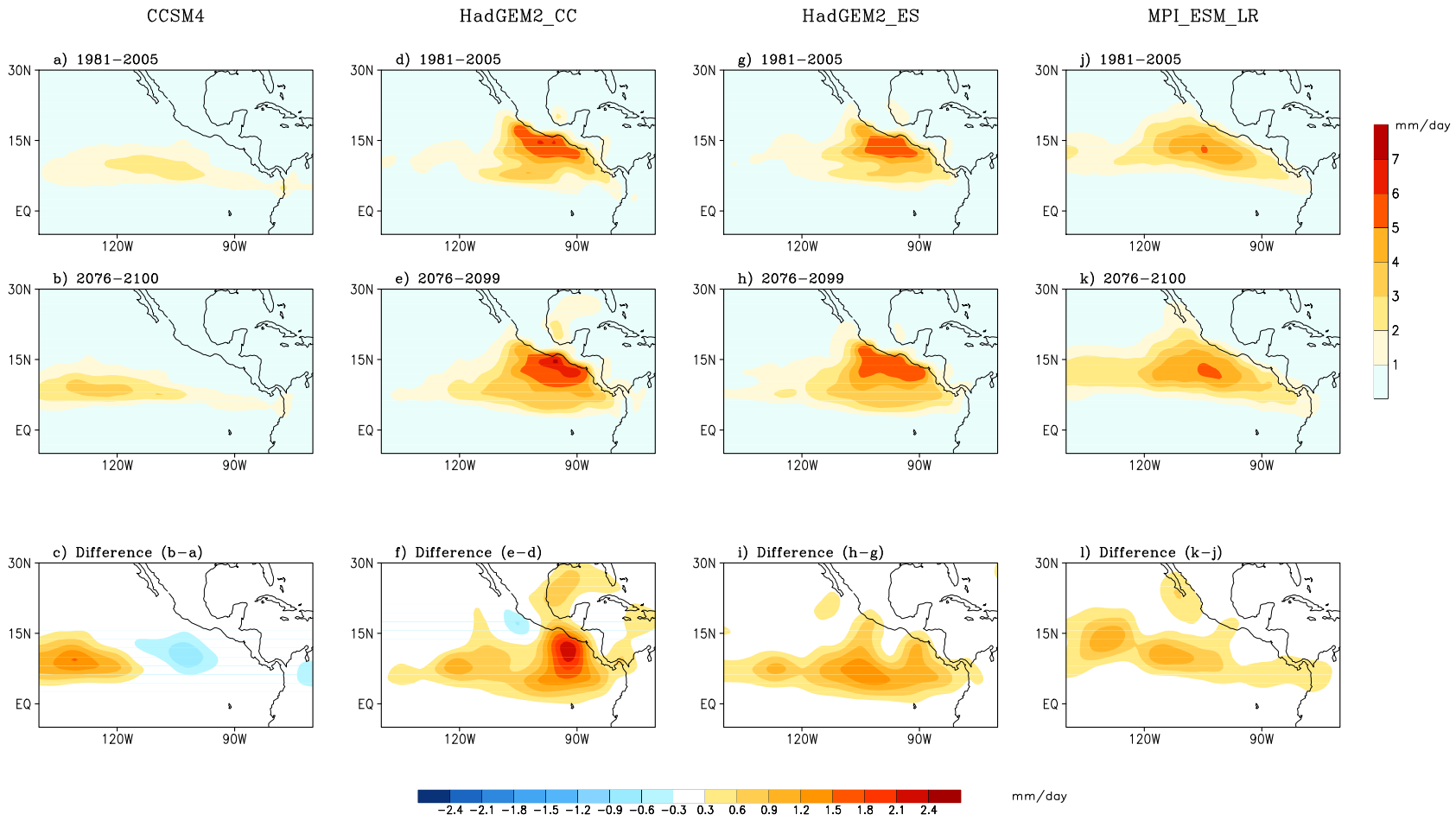

Figure 13 Spatial distributions of CEOF1 amplitude of summer rainfall over the ENP based on four CMIP5 models in historical simulations (upper panels) and future projections under the RCP 8.5 scenario (middle panels) and their differences (lower panels)